Thermal stability and corrosion resistance of nanocrystallized zirconium formed by surface mechanical attrition treatment

Yong Han[a] and Lan Zhang
State Key Laboratory for Mechanical Behavior of Materials, Xi'an Jiaotong University, Xi'an 710049, China

Jian Lu
Department of Mechanical Engineering, The Hong Kong Polytechnic University, Hung Kom, Kowloon, Hong Kong, China

Wengting Zhang
State Key Laboratory for Mechanical Behavior of Materials, Xi'an Jiaotong University, Xi'an 710049, China

(Received 9 February 2009; accepted 17 June 2009)

The thermal stability and corrosion behavior of the nanostructured layer on commercially pure zirconium, produced by surface mechanical attrition treatment (SMAT), were investigated. It is indicated that the nanograined Zr is stable at annealing temperatures up to 650 °C, above which significant grain growth occurs and the grain size shows parabolic relationship with annealing time. The activation energy for grain growth of the nanograined Zr is 59 kJ/mol at 750–850 °C, and the grain growth is dominated by grain-boundary diffusion. The as-SMATed nanograined Zr exhibits higher corrosion resistance than the 550–750 °C annealed SMATed Zr and the unSMATed coarse-grained Zr. It is indicated that the corrosion resistance of Zr tends to increase with the reduction of grain size, which is related to the dilution of segregated impurities at grain boundaries due to grain refinement and the formation of passive protection film.

I. INTRODUCTION

Ultrafine grained (UFG, 1–1000 nm) materials are of great interest due to their unique physical, mechanical, and biological properties relative to coarse-grained counterparts.[1–5] The issues of thermal stability and corrosion in UFG materials are important for two primary reasons. First, because on the basis of a Gibb's free energy argument, such fine grains may be metastable, and hence prone to coarsening with a low energy threshold. Second, engineering applications require the consolidation of UFG materials, which typically involves exposure to elevated temperature or corrosive environment. A number of investigations on the thermal stability of UFG materials have been carried out, and the findings reveal that in pure metals produced by severe plastic deformation (SPD), significant grain growth occurs at a relatively low temperature of 0.31 to 0.34 *Tm* (where *Tm* is the melting temperature in K).[6–8] Although significant grain growth in UFG Ti formed by equal channel angular pressing was reported to occur at 400 °C (0.34 *Tm*),[8] it is worth noticing that no significant grain growth was observed in cryomilled *nc*-Ti at the annealing temperature between 450 and 720 °C, keeping grain size from 15.2 to 27.5 nm.[9] In the case of multicomponent systems, metallic alloys such as Al–Mg,[10] Ni-based alloys,[11] and Ti–24Nb–4Zr–7.9Sn alloy[12] had a relatively high critical temperature, with slow to significant grain growth between 0.5 to 0.65 *Tm*, due to the barrier effect of two-phase duplex microstructure on grain growth. It is indicated that the thermal stability of UFG metallic materials is strongly dependent on the kinds of metals and formation techniques.

Relative to thermal stability, the reports on corrosion behaviors of SPD-derived UFG metallic materials are limited, and the results are not consistent. For copper, Vinogradov et al.[13] reported that corrosion behavior of UFG copper did not qualitatively change in comparison with its coarse-grained one in the modified Livingston etchant (HCl: 30 mL + CH_3COOH: 10 mL + H_2O: 410 mL) at the constant temperature of 298, 303, 308, and 313 K. Miyamoto et al.[14] revealed that UFG copper exhibited an improved corrosion resistance relative to coarse-grained copper in the modified Livingston etchant (HCl: CH_3COOH: H_2O = 1: 3: 80) at ambient temperature, whereas Barbucci et al.[15] showed a decrease in the protective properties of the passive layer in the nanograined Cu89Ni09 alloy in 0.3% Na_2SO_4 solution added with different chloride at room temperature (RT). For titanium, it was found that the UFG Ti was more resistant to corrosion than its coarse-grained counterpart in H_2SO_4

[a]Address all correspondence to this author:
e-mail: yonghan@mail.xjtu.edu.cn
DOI: 10.1557/JMR.2009.0368

solution concentrations from 1 to 5 M at RT[16]; on the contrary, a lower corrosion resistance of UFG Ti in comparison with the coarse-grained Ti in 0.9% NaCl at RT was revealed by Garbacz et al.[17] In the case of metallitic alloys, UFG Al–Mn alloy in 3.5% NaCl at RT[18] and AISI-321 stainless steel in 3.5% NaCl at RT[19] possessed a better corrosion resistance than their coarse-grained counterparts; however, a negative efficiency of grain refinement to corrosion resistance in AZ61 magnesium alloy in 0.9% NaCl at RT was also reported.[20] It is suggested that the effect of grain refinement on corrosion resistance is changeable in different metallic systems.

Zirconium and its alloy have been extensively used as cladding materials for fuel element in nuclear reactor systems, which involves an acid and high-temperature environment.[21] Due to the beneficial properties of UFG metals, efforts to produce UFG or nanograined Zr have been undertaken recently by severely rolling,[5] and surface mechanical attrition treatment (SMAT).[22] The basic principle of SMAT is the generation of plastic deformation in the surface layer of a bulk metal by means of the repeated multidirectional impact of flying balls on the sample surface. The plastic deformation in the surface layer under the high strain rate results in a progressive refinement of coarse grains into a nanometer regime. As described in our previous work,[22] the grain size of Zr increases gradually from about 5 to 10 nm at the top surface to about of 100 nm at a depth of 20 μm from the treated surface after treatment for 30 min. Although a theoretic simulation showed that the corrosion rate of Zr decreased with the decrease of grain size,[23] experimental investigation of thermal stability and corrosion resistance of the nanograined Zr has been rarely reported, which is the purpose of this work.

II. MATERIALS AND EXPERIMENTAL METHODS

The as-received commercially pure Zr plates, which had a purity of 99.99 wt% were annealed at 550 °C for 10 h to eliminate residual deformation. After annealing, they were ground to remove oxide and polished to a mirror finish. For SMAT of the Zr plate, an SNC-II surface nanocrystallization testing machine, as described in detail elsewhere,[24] was used. A Zr plate with diameter of 100 mm and thickness of 5 mm was mounted at the top, while zirconia balls (2 mm in diameter) were placed at the bottom of a cylinder-shaped vacuum chamber in the machine. The bottom of the chamber was vibrated by a vibration generator at a frequency of 20 kHz, resulting in the balls resonating and impacting the surface of the Zr plate. Under this condition, the Zr plate was treated at RT for 15 min.

To study the thermal stability of the nanograined Zr, the samples cut from the SMATed Zr plate were encapsulated in quarts tubes with a vacuum of 1.5×10^{-4} Pa to receive annealing treatment at 250, 350, 450, 550, 650, and 750 °C for 10 h, respectively. Hardness measurements were performed on the surfaces of the SMATed samples annealed at different temperatures by a MVK-H300V Vickers hardness testing machine (Tianxing, Shenyang, China), with a load of 20 g and a loading time of 5 s. X-ray diffraction (XRD) patterns of the annealed SMATed samples were collected using Cu K_α radiation in θ–2θ mode over a 2θ angle of 20° to 80° at a step of 0.017°. The grain sizes of the surface layers and specific depth layers from the surfaces of the annealed SMATed samples were observed by transmission electron microscopy (TEM; JEM-2100F, JEOL, Tokyo, Japan) operated at 200 kV. TEM foils for the layers at different depths from the surfaces of the annealed SMATed samples were prepared first by removing the corresponding surface layers, and then mechanically grinding the samples on the unSMATed sides to get thin plates with a thickness of about 30 μm; the thin plates were then electropolished using a twin-jet technique in a solution of 10% perchloric acid and methanol at a voltage of 50 V and a temperature of −40 °C. Furthermore, the TEM foil taken from the SMATed surface layer was set on a Gatan 628 single-tilt heating holder (Tokyo, Japan) equipped in the JEM-2100F TEM (JEOL) and in situ observation of the grain growth was performed at 750 and 850 °C for different duration times of 5 to 70 min. At each duration time, more than 5 bright-field image pictures were taken, the measurements of the grain sizes were made directly from TEM photomicrographs and at least 300 grains were measured to count the average grain size. Because many grains are elongated, the datum points were separately presented for measurements of the average of the short axis, the average of the long axis, and the average from randomly selected directions, whereas measurements for the grains were taken consistently along randomly selected directions, as described by Wu et al.[25]

Potentiodynamic tests of the unSMATed, as-SMATed, and 550–750 °C annealed SMATed Zr samples were performed using an IM6e potentiostat system (Zahner, Germany) at RT. In the tests, each of the samples with an exposed area of 1 cm^2 was immersed in a 1 N H_2SO_4 solution under an open laboratory air condition, and a platinum electrode was used as a counter. All electrochemical potential measurements were taken with respect to a saturated calomel electrode (SCE). After a 30 min delay under open-circuit conditions to make the samples reach a steady state, the potentiodynamic polarization curves were measured from −0.5 to +1.5 V potential (referred to the SCE) at a scan rate of 0.5 mV/s. Furthermore, the surface morphologies of the potentiodynamic polarized samples were observed by a field-emission scanning electron microscope (FE-SEM; JSM-6700F, JEOL). The elements composition was examined by an energy dispersive x-ray spectrometer (EDX; DX-4, Philips, The Netherlands).

III. RESULTS

A. Thermal stability of the nanostructured surface layer

Figure 1 shows XRD patterns of the SMATed samples annealed at different temperatures for 10 h. Compared with the as-SMATed sample, the 250 °C annealed sample exhibits a slight sharpening of the diffraction peaks. On the other hand, there is no obvious change in full width at half maximum (FWHM) and intensity for the diffraction patterns of the samples annealed 250–550 °C; however, the diffraction peaks of the samples annealed at 650 and 750 °C are apparently sharpened and their intensities become strong, as shown in Table I, in which (110) plane was taken as an example. Surface hardness values of the SMATed-samples annealed at different temperatures for 10 h are shown in Fig. 2. The hardness almost does not change at the annealing temperature lower than 550 °C, but then tends to decrease with further increasing the annealing temperature 650 to 750 °C, suggesting that significant grain growth occurs from 650 °C. The error bars for grain size and hardness data in Fig. 2 are standard deviations.

On the basis of the XRD and hardness analysis results, the microstructure observation was performed by TEM on the SMATed-samples annealed at 250 to 750 °C for 10 h with emphasis on 550, 650, and 750 °C. The TEM images of the as-SMATed and 550 °C annealed surface layers are shown in Fig. 3. Bright-field images [Figs. 3(a) and 3(c)] and dark-field images [Figs. 3(b) and 3(d)] indicate that the as-SMATed surface layer is nanocrystallized with a grain size of about 7 nm, and no obvious changes in grain size and morphology are observed after annealing at 550 °C; in addition, selected-area electron diffraction (SAED) patterns [inset in Figs. 3(a) and 3(c)] all exhibit continuous rings without spots, which is an electron diffraction characteristic of very fine grains. However, the 550 °C annealed sample exhibits a decrease of defect density in comparison with the as-SMATed sample. Figure 4 shows inverse Fourier high-resolution TEM (HRTEM) images of the as-SMATed and 550 °C annealed surface layers. In the as-SMATed surface layer, dislocations with the density of about $6 \times 10^{16}/m^2$ are visible along the grain boundaries but not in the grain interiors, because dislocations will hardly pileup in grains when grain sizes are less than a critical value as suggested elsewhere[22,26]; after annealing, the dislocation density at grain boundaries decreases. The *d*-spacing of (100) plane keeps constant at 0.277–0.279 nm before and after annealing, fitting well to that presented in JCPDS Card No. 5-665 (0.2798 nm). Figure 5 shows TEM micrographs of the layers at a depth of 10 μm from the surfaces of the as-SMATed and 550 °C annealed samples. In the layers, grains are near-equiaxed with sizes of about 60 to 80 nm, and reduced dislocation density in the interiors of the

TABLE I. Peak intensity and FWHM of (110) plane detected from XRD spectra of the different samples.

Samples	(110) plane	
	Peak intensity (a.u.)	FWHM (°)
As-SMAT Zr	423	0.41
SMATed Zr annealed at 250 °C for 10 h	435	0.40
SMATed Zr annealed at 450 °C for 10 h	440	0.40
SMATed Zr annealed at 550 °C for 10 h	505	0.37
SMATed Zr annealed at 650 °C for 10 h	1325	0.19
SMATed Zr annealed at 750 °C for 10 h	2273	0.17

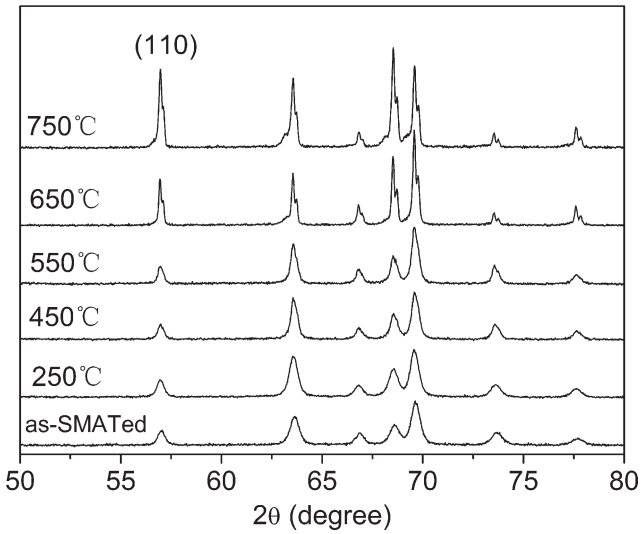

FIG. 1. XRD patterns of the SMATed samples annealed at different temperatures for 10 h.

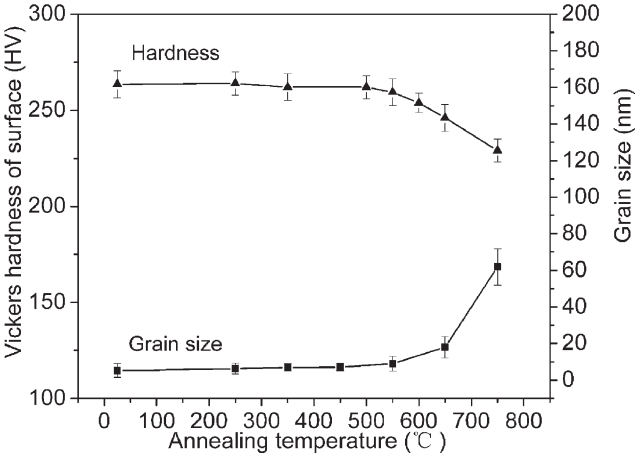

FIG. 2. Surface hardness values of the SMATed-samples annealed at different temperatures for 10 h, together with TEM-determined average grain sizes of the annealed surface layers.

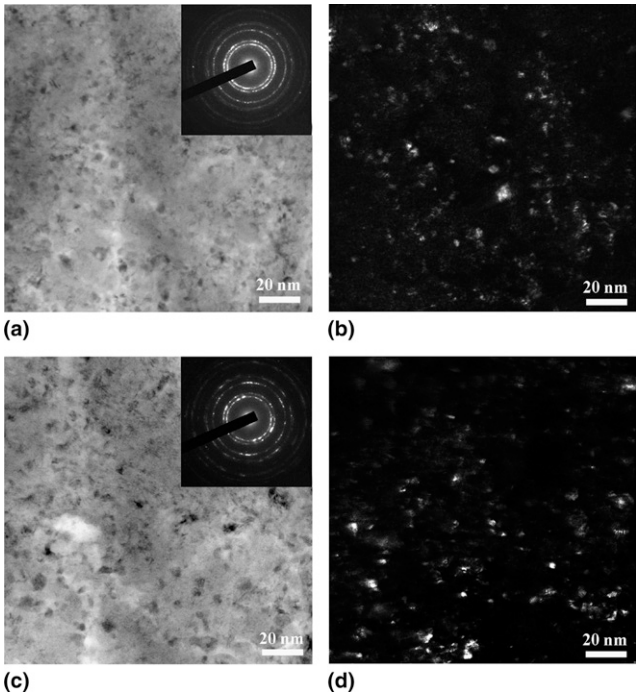

FIG. 3. (a) Bright-field and (b) dark-field images of the as-SMATed surface layer; (c) bright-field and (d) dark-field images of the 550 °C annealed surface layer.

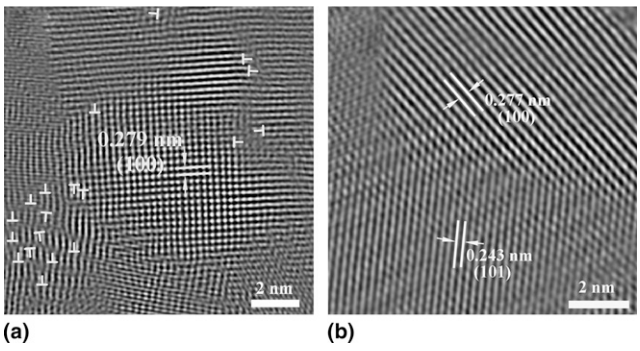

FIG. 4. Inverse Fourier HRTEM images of the (a) as-SMATed and (b) 550 °C annealed surface layers.

annealed grains can be observed. It is suggested that annealing of the SMATed sample at 550 °C for 10 h does not alter the grain size but results in a decrease of dislocation density in the nanocrystalline layer. However, annealing at an elevated temperature leads to grain growth, as shown in Fig. 6. The grains in the surface layer become equiaxed with an average size of 18 ± 8 nm after annealing at 650 °C and significantly increase to 65 ± 10 nm in average size after annealing at 750 °C. Furthermore, an SAED pattern of the 750 °C annealed surface layer [inset in Fig. 6(b)] presents separate spots instead of continuous rings, further confirming that the grains grow up apparently at the annealing condition. The TEM-determined average grain sizes of the annealed surface layers at different temperatures are also plotted in Fig. 2. In combination

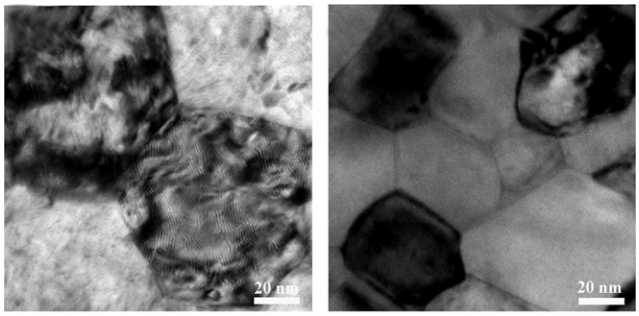

FIG. 5. TEM micrographs of the layers at the depth of 10 μm from the surfaces of the (a) as-SMATed and (b) 550 °C annealed samples.

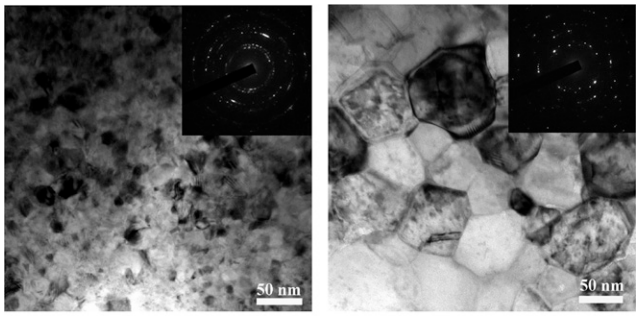

FIG. 6. TEM micrographs of the surface layers of the SMATed samples annealed at (a) 650 °C and (b) 750 °C for 10 h.

with the XRD, hardness, and TEM results, it is indicated that the significant grain growth temperature of the SMAT-derived nanocrystalline Zr is about 650 °C (923 K), e.g., 0.43 *Tm* (*Tm* of Zr is known as 2128 K). This result suggests that SMAT-derived nanocrystalline Zr displays a high resistance against grain growth as compared with other SPD-derived UFG metals, such as Cu, Ti, Cr,[5–7] and cold-worked Zircaloy-4.[27]

In situ TEM-determined average grain sizes of the SMATed surface layers held at 750 and 850 °C for different duration times are shown in Fig. 7, and the corresponding TEM images taken from the 750 °C held surface layer, as an example, are shown in Fig. 8. It is indicated that the relationships between average grain size and duration time at 750 and 850 °C are parabola, and temperature is a key factor to control grain growth. As the temperature reaches 850 °C, grain size of the surface layer increases significantly in a short period of time, for instance, to 55 ± 5 nm after 1 h duration.

B. Corrosion behaviors

Figure 9 shows potentiostatic polarization curves of the unSMATed Zr, as-SMATed sample, and SMATed samples annealed at 550, 650, and 750 °C for 10 h. The curves of the as-SMATed and annealed SMATed-samples exhibit active/passive transient peaks on anode sides (marked with arrows in Fig. 9), revealing typical

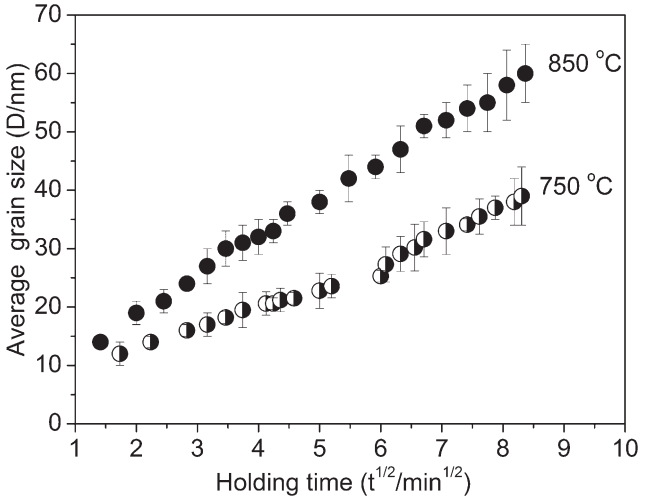

FIG. 7. In situ TEM-determined average grain sizes of the SMATed surface layers versus different annealing times ($t^{1/2}$) at 750 and 850 °C.

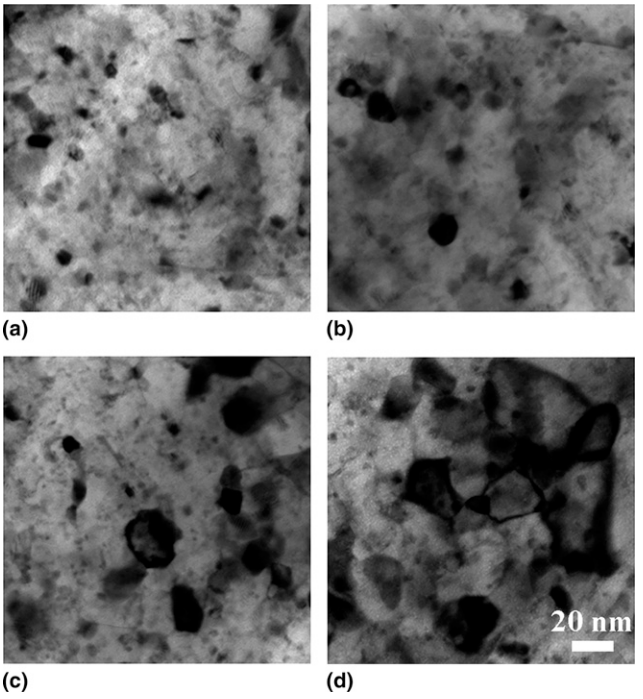

FIG. 8. In situ TEM images of the SMATed surface layer held at 750 °C for duration time of (a) 5 min, (b) 15 min, (c) 30 min, and (d) 45 min.

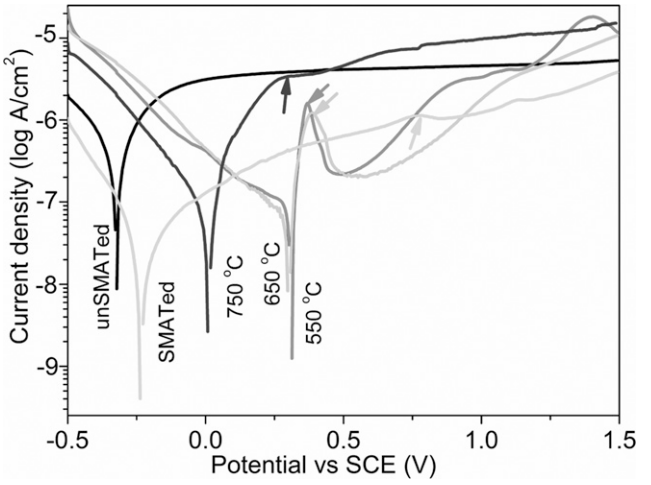

FIG. 9. Potentiostatic polarization curves of the unSMATed sample, as-SMATed sample, and SMATed-samples annealed at 550, 650, and 750 °C for 10 h.

TABLE II. Corrosion potentials (E_{cor}) and corrosion current densities (I_{cor}) of the different samples.

Samples	Grain size (nm)	E_{cor} (V)	I_{cor} (A/cm^2)
unSMATed Zr	$10 \pm 5 \times 10^3$	−0.32	5.3×10^{-7}
SMATed Zr	7 ± 3	−0.23	3.2×10^{-8}
SMATed Zr annealed at 550 °C for 10 h	8 ± 4	0.31	7.8×10^{-8}
SMATed Zr annealed at 650 °C for 10 h	18 ± 6	0.30	7.5×10^{-8}
SMATed Zr annealed at 750 °C for 10 h	65 ± 10	0.01	1.5×10^{-7}

passivation characteristics; however, such active/passive transient peaks do not appear in the polarization curve of unSMATed Zr in which the corrosion-current density on the anode side rapidly increases with potential until it reaches a platform. The corrosion potentials and corrosion current densities of the samples, derived from the potentiostatic polarization curves, are shown in Table II, together with grain size. The unSMATed sample has the most negative corrosion potential, and the annealed SMATed-samples show more positive corrosion potentials compared with the as-SMATed sample. As known, the corrosion potential does not provide much insight into corrosion rates.[28] It is worth noting that the as-SMATed sample reveals the lowest corrosion-current density, and the corrosion current densities of the 550 and 650 °C annealed SMATed-samples are similar, which are about one order of magnitude smaller than that of the unSMATed sample. Although the 750 °C annealed SMATed-sample with significantly growing grains to about 65 nm and exhibits higher corrosion-current density than the 550 and 650 °C annealed SMATed-samples, its corrosion-current density is still lower than that of the unSMATed sample.

The corroded surfaces of the unSMATed Zr, as-SMATed sample, 550 and 750 °C annealed SMATed-samples after potentiodynamic polarization are shown in Fig. 10. For the unSMATed Zr, many corrosion pits along grain boundaries are clearly visible: some grains have been selectively attacked while others remain intact by environment. This selective corrosion of grains is attributed to the difference of surfaces crystallographic orientation. For the as-SMATed sample, however, it is noticeable that there are few localized corrosion pits on its surface, but the pits are also inconspicuous in size and the surface is rather smooth, so that the degree of local environmental

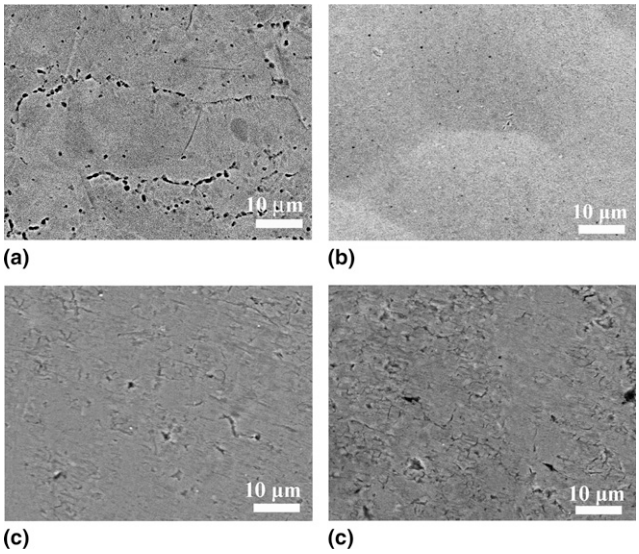

FIG. 10. SEM micrographs of the corroded surfaces after potentiodynamic polarization tests: (a) unSMATed sample, (b) as-SMATed sample, SMATed samples annealed at (c) 550 °C and (d) 750 °C for 10 h.

attack at grain boundaries is small. Similarly, for the annealed SMATed-samples at 550 °C, pitting occurs in a lower probability, and the pits are smaller and flatter than that in the unSMATed Zr. Nevertheless, on the surface of the 750 °C annealed SMATed-sample, for which nanograins have significantly grown, big and deep corrosion pits are more and clearly visible [Fig. 10(d)]. In combination with Figs. 9 and 10, it is indicated that the corrosion resistance of the present samples in the H_2SO_4 solution are in the following order: as-SMATed Zr > annealed SMATed Zr > unSMATed coarse-grained Zr (with grain size of about 10 μm), appearing to be consistent with the report given by Vinogradov et al. that the UFG Ti was more resistant to corrosion than its coarse-grained counterpart[16]; on the other hand, the corrosion resistance of the annealed SMATed Zr tend to decrease with the increase of grain size (e.g., annealing temperature).

IV. DISCUSSION

A. Thermal stability

A deformed metal contains a large stored energy and, on annealing at elevated temperatures, will normally revert to a lower energy state by means of recovery, recrystallization (a nucleation and growth phenomenon), and grain growth.[9,29] In this work, a decrease of dislocation density in the annealed nanocrystalline layer was observed (Figs. 4 and 5), suggesting that recovery occurs during annealing at elevated temperature. A slight sharpening of the XRD peaks of the 250 °C annealed sample as compared to the as-SMATed sample (Fig. 1) indicates that recovery of the SMATed nanostructure might start at 250 °C. This is consistent with the result revealed in shot-peened micrometer-sized Zr.[30] However, recrystallization of the SMATed nanostructure does not happen during annealing at 250 to 550 °C because no drop of the average grain size was observed. The SMATed nanograined Zr is stable until 650 °C and exhibits a higher critical temperature of 0.43 *Tm* relative to SPD-derived UFG Cu, Ti, and Cr.[5–7] It is known that high thermal stability of cryomilled nanograined Ti results from a recrystallization process due to the reordering of cryomilling-introduced nitrogen atoms in octahedral interstices in Ti.[9] For cold-rolled Ti–24Nb–4Zr–7.9Sn alloy, the formation of the α−phase during annealing and the pinning effect of the α precipitates on grain boundaries significantly improves the thermal stability of the nanostructure up to 0.5 *Tm*.[12] The reason for the SMATed nanograined Zr to be of a relatively higher critical temperature is not well understood at present, and may be due to a much higher melting point of Zr than the aforementioned pure metals.

Grain coarsening in nanostructured metals can be driven by stress and temperature. It is reported that the stress-driven grain coarsening might be due to either one or a combination of the grain boundary migration and the grain rotation.[31,32] For the temperature-driven grain growth, a classical expression relating the average grain size D and time t under the isothermal annealing condition is[33–35]:

$$D - D_0 = kt^{1/n} \quad , \tag{1}$$

where D_0 is the initial grain size, D is the grain size after annealing for a time period of t, n is the grain growth exponent, k characterizes the grain growth rate at a given temperature having an Arrhenius relation with temperature:

$$k = k_0 \exp\left\{\frac{-Q}{RT}\right\} \quad , \tag{2}$$

where R is the molar gas constant, T the absolute temperature, Q the activation energy for grain growth, and k_0 is a constant. Following Eq. (1), it is known that grain growth processes are dominated by curvature-driven grain boundary migration when n = 2, volume diffusion when n = 3, and stochastic jumping of atoms across the grain boundaries if n = 4, respectively.[33–35]

On the basis of the measured average grain sizes of the SMATed surface layers held at 750 and 850 °C for different times, plots of ln(D–D_0) versus ln(t) at the temperatures were drawn in Fig. 11, showing the grain growth kinetics of the nanocrystalline Zr as

$$D - D_0 = 3.5t^{1/2} \quad \text{at } 750\ ^\circ\text{C} \quad ,$$

$$D - D_0 = 6.5t^{1/2} \quad \text{at } 850\ ^\circ\text{C} \quad .$$

It is indicated that the grain growth rates k (nm/min$^{1/2}$) are 3.5 at 750 °C and 6.5 at 850 °C, respectively, and the

growth exponent n is 2, suggesting that the growth of the nanograins in the SMATed Zr is dominated by the mechanism of curvature-driven grain boundary migration.[33–35] Inputting the measured values of k into Eq. (2), the calculated activation energy for the grain growth is 59 kJ/mol in the temperature range from 750 to 850 °C, which is lower than that of Cold-Worked Zircaloy-4.[36] As known, two diffusion mechanisms may be considered for the grain growth process: diffusion through lattice or by grain boundary. It is reported that the activation energies for lattice self-diffusion in micrometer-sized Zr approaches 275 kJ/mol.[37] Furthermore, grain boundary self-diffusion measurements by Vieregge et al.[38] on pure polycrystalline-zirconium indicated a constant activation energy of 167 kJ/mol from 500 to 862 °C. The activation energy disagreement between the present experimental result and the literature is thought to be related to the difference in the grain boundary structure between nanostructured and coarse-grained materials. There are experimental evidences for the presence of high nonequilibrium grain boundaries (e.g., boundaries with long-range stresses and excess energy) in UFG materials prepared by severe plastic deformation.[39,40] By measuring the grain size at different strains of compressed Cu, Valiev et al. reported that the activation energy for grain growth was much lower than that of grain-boundary diffusion due to enhanced atomic mobility associated with the nonequilibrium grain boundaries.[41] Similar results were also reported for cryomilled *nc*-Ti,[9] cold-rolled Ti–24Nb–4Zr–7.9Sn alloy,[12] severely deformed Mg–Al alloys,[41] and electrodeposited nanocrystalline gold.[42] It is expected that the nonequilibrium grain boundaries in the SMATed Zr increase atomic mobility and result in the abnormal low Q value. This suggests that the grain growth in the present nanograined Zr is dominated by grain boundary diffusion, similar to what is observed in nanograined Cu.[39,40]

B. Corrosive behaviors

Intergranular corrosion is often induced by impurity segregation and precipitation at grain boundaries. On the other hand, defects such as dislocations and grain boundaries have also intrinsic susceptibility to local attack, and reactivity of these defects increases with increasing extra free energy associated with intrinsic structural disorder.[43] In the present work, the as-SMATed nanograined Zr and the annealed nanograined Zr exhibit a higher corrosion resistance than the unSMATed coarse-grained Zr, and the corrosion resistance of the annealed nanograined Zr decreases with the increase of annealing temperature. This is related to the dilution of segregated impurities at grain boundaries due to grain size reduction and the change of dislocation density caused by annealing.

EDX analysis shown in Fig. 12 indicates that the detected impurities in the unSMATed zirconium are C, Hf, and Re, and C has a higher concentration on grain boundaries than in grain interior of the coarse-grained Zr. Such segregation of impurities to grain boundaries was also observed by Balyanov et al.[16] in commercially pure CG Ti, showing that the Al and Fe contents were about 40% and 470%, respectively, higher on grain boundary than in grain interior. The segregation of impurities to grain boundaries in the coarse-grained Zr could accelerate its intergranular corrosion, similar to that reported by Balyanov et al.[16] Palumbo et al.[44] estimated content of segregated impurities at grain boundaries assuming the complete segregation. When grain size is decreased from 10 to 0.3 μm, segregated impurities are estimated to be diluted by about 1/30.[44] Dilution of segregated impurities at grain boundaries is a

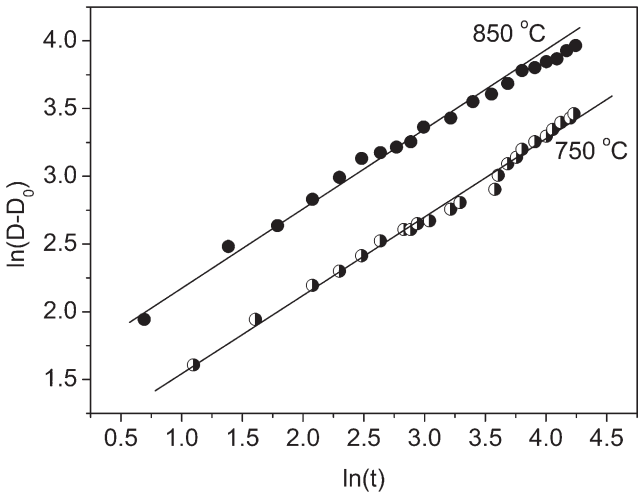

FIG. 11. Plot of $\ln(D-D_0)$ versus $\ln(t)$ for holding temperatures of 750 and 850 °C.

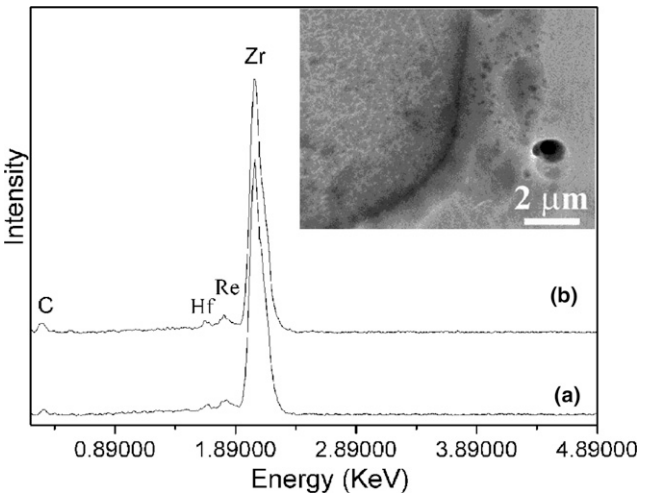

FIG. 12. EDX spectra measured at (a) grain interior and (b) grain boundary of unSMATed Zr.

well-known beneficial effect of grain size reduction for corrosion resistance. Because the grain sizes of the present samples are in the order: as-SMATed Zr < annealed SMATed Zr ≪ unSMATed Zr, in combination of the report and Fig. 10, it is expected that intergranular corrosion can be reduced in both the as-SMATed Zr and the annealed SMATed Zr due to the dilution of segregated impurities at grain boundaries in comparison with the unSMATed Zr. For the annealed SMATed samples, the grain sizes of the 550–650 °C annealed samples still keep fine (less than 20 nm), whereas the 750 °C annealed Zr exhibits significant grain growth to about 65 nm; this results in enhancement of impurities segregation at grain boundaries and thereby a decrease of corrosion resistance of the 750 °C annealed Zr relative to the 550–650 °C annealed samples.

The electrochemical corrosion of metal in the anode side of polarization includes two processes, e.g., electrochemical dissolution and passivation.[45] Corrosion performance of a metal is not only determined by its dissolution rate but also depends on its passivation ability. During the process of electrochemical dissolution, spontaneous dissolution in the acid solution and compelling dissolution under the effect of external electrical field take place simultaneously.[45] In the case of Zr anode, both of the dissolution reactions obey to the following equation[46]:

$$\mathrm{Zr}(m) = \mathrm{Zr}^{4+}(aq) + 4e^{-} \quad .$$

In thermodynamic consideration, the extra free energy lowers half-cell electrode potential, resulting in a greater tendency for electrochemical dissolution in certain corrosive environments. Beaunier et al.[47,48] proposed an atomic-scale model, which describes the penetration rate at grain boundaries, using activation energy for dissolution and activation energy for the formation of an active site for passivation, and suggested that the dissolution rate of the surface intersecting with the grain boundaries was higher than that in the grain interiors. Erb et al.[49] and Miyamoto et al.[14] also reported that the dissolution rate at nonequilibrium grain boundaries with extrinsic dislocations should be higher than that at equilibrium grain boundaries, because excess extrinsic dislocations near the grain boundaries provide more active sites with lower activation energy for dissolution. As shown in Fig. 4(a), the present as-SMATed nanograined Zr has a large amount of nonequilibrium grain boundaries with high dislocation density. Thus, a larger area of grain boundaries due to grain refinement leads to high compelling dissolution of the as-SMATed Zr in H_2SO_4 solution at a relatively low corrosion potential. However, corrosion potential just reflects a value at which anode polarization occurs.[45]

On the other hand, similar to titanium, zirconium is an easily passivated metal during the electrochemical corrosion process.[46,50] Once passivation occurs, the formed passive film acts as a barrier to reduce the dissolution of zirconium, preventing its further corrosion. As known, passivation ability is related to active sites for passivation, and a high density of defects such as grain boundaries and dislocations on the surface is a benefit to the formation of passive film.[51–54] For example, Movchan et al.[51] found the SPD-derived ultrafine-gained Ti could form a passive surface more readily than coarse-grained Ti. Johansen et al.[52] reported that passive film could be formed at a greater rate on deformed Ti (34% plastic strain) than on high temperature annealed deformed Ti, and passivation first started on the surface of crystalline lattice defects. Furthermore, it has also been reported that the high-density grain boundaries could enhance the adhesion between the passive film and the surface due to the increase in the electron activity at grain boundaries and possible pegging of the passive film into grain boundaries.[16,53,54] According to the previous works,[51–54] the present as-SMATed nanograined Zr with a large amount of nonequilibrium grain boundaries and high dislocation density, as shown in Fig. 4(a), would have a higher density of nucleation sites for passive films during the corrosion process, and the formed passive film could be more readily and adhesive than for the unSMATed sample. After annealing the SMATed Zr, the number of active passivation sites such as dislocations and grain boundaries in the 550–750 °C annealed SMATed Zr tend to reduce with increasing the annealing temperature (Fig. 4). It is expected that the adhesion between the passive films and the 550–750 °C annealed SMATed Zr would become weak with increasing the annealing temperature, leading to the decrease of corrosion resistance of the SMATed Zr annealed at elevated temperature, especially for the 750 °C annealed sample.

V. CONCLUSION

A nanograined layer has been produced on commercially pure zirconium using SMAT. The SMAT-derived nanograins with a size of 7 nm are free of dislocations in grain interiors but have high dislocation density along grain boundaries. The nanograined Zr is thermally stable at annealing temperatures up to 650 °C, above which significant grain growth occurs and the average grain size shows a parabolic relationship with annealing time. The activation energy for grain growth of nanograined Zr is about 59 kJ/mol at 750 to 850 °C, and the grain growth is dominated by grain-boundary diffusion. The as-SMATed nanograined Zr exhibits higher corrosion resistance than the 550–750 °C annealed SMATed Zr and the unSMATed coarse-grained Zr. It is indicated that the corrosion resistance of Zr tends to increase with the reduction of grain size, which is related to the dilution of segregated impurities at grain boundaries due to

grain refinement and the formation of passive protection film.

ACKNOWLEDGMENTS

We appreciate the National High Technology Research and Development Program of China (Grant No. 2006AA03Z0447) and National Natural Science Foundation of China (Grant Nos. 50571079, 50671078) for financially supporting this work.

REFERENCES

1. H. Gleiter: Nanostructured materials: Basic concepts and microstructure. *Acta Mater.* **48,** 1 (2000).
2. R.Z. Valiev, R.K. Islamgaliev, and I.V. Alexandrov: Bulk nanostructured materials from severe plastic deformation. *Prog. Mater. Sci.* **45,** 103 (2000).
3. S.C. Tong and H. Chen: Nanocrystalline materials and coatings. *Mater. Sci. Eng., R* **45,** 1 (2004).
4. D.B. Witkin and E.J. Lavernia: Synthesis and mechanical behavior of nanostructured materials via cryomilling. *Prog. Mater. Sci.* **51,** 1 (2006).
5. L. Saldana, A. Méndez-Vilasc, L. Jiang, M. Multignerd, J.L. González-Carrasco, M.T. Pérez-Prado, M.L. González-Martín, L. Munuera, and N. Vilaboa: In vitro biocompatibility of an ultrafine grained zirconium. *Biomaterials* **28,** 4343 (2007).
6. R.K. Islamgaliev, F. Chmelik, and R. Kuzel: Thermal stability of submicron grained copper and nickel. *Mater. Sci. Eng., A* **237,** 43 (1997).
7. V.V. Stolyaro, Y.T. Zhu, I.V. Alexandrov, T.C. Lowe, and R.Z. Valie: Grain refinement and properties of pure Ti processed by warm ECAP and cold rolling. *Mater. Sci. Eng., A* **343,** 43 (2003).
8. R. Wadsack, R. Pippan, and B. Schedler: Structural refinement of chromium by severe plastic deformation. *Fusion Eng. Des.* **66,** 265 (2003).
9. F. Sun, A. Zuniga, P. Rojas, and E.J. Lavernia: Thermal stability and recrystallization of nanocrystalline Ti produced by cryogenic milling. *Metall. Mater. Trans.* **37,** 2069 (2006).
10. M. Lewandowska and K.J. Kurzydyowski: Thermal stability of a nanostructured aluminium alloy. *Mater. Charact.* **55,** 395 (2005).
11. M.R. Shankar, B.C. Rao, S. Chandrasekar, W.D. Compton, and A.H. King: Thermally stable nanostructured materials from severe plastic deformation of precipitation-treatable Ni-based alloys. *Scr. Mater.* **58,** 675 (2008).
12. S.J. Li, Y.W. Zhang, B.B. Sun, Y.L. Hao, and R.T. Yang: Thermal stability and mechanical properties of nanostructured Ti–24Nb–4Zr–7.9Sn alloy. *Mater. Sci. Eng., A* **480,** 101 (2008).
13. A. Vinogradov, T. Mimaki, S. Hashimoto, and R.Z. Valiev: On the corrosion behavior of ultra-fine grain copper. *Scr. Mater.* **41,** 319 (1999).
14. H. Miyamoto, K. Harada, T. Mimaki, A. Vinogradov, and S. Hashimoto: Corrosion of ultra-fine grained copper fabricated by equal-channel angular pressing. *Corros. Sci.* **50,** 1215 (2008).
15. A. Barbucci, G. Farnen, P. Matteazzi, and R. Riccieri: Corrosion behavior of nanocrystalline $Cu_{90}Ni_{10}$ alloy in neutral solution containing chlorides. *Corros. Sci.* **41,** 463 (1999).
16. A. Balyanov, J. Kutnyakova, N.A. Amirkhanova, V.V. Stolyarov, R.Z. Valiev, X.Z. Liao, Y.H. Zhao, Y.B. Jiang, H.F. Xu, T.C. Lowe, and Y.T. Zhu: Corrosion resistance of ultra fine-grained Ti. *Scr. Mater.* **51,** 225 (2004).
17. H. Garbacz, M. Pisarek, and K.J. Kurzydłowski: Corrosion resistance of nanostructured titanium. *Biomol. Eng.* **24,** 559 (2007).
18. W. Wei, K.X. Wei, and Q.B. Du: Corrosion and tensile behaviors of ultra-fine grained Al–Mn alloy produced by accumulative roll bonding. *Mater. Sci. Eng., A* **454–455,** 536 (2007).
19. B.N. Mordyuk, G.I. Prokopenko, M.A. Vasylyev, and M.O. Iefimov: Effect of structure evolution induced by ultrasonic peening on the corrosion behavior of AISI-321 stainless steel. *Mater. Sci. Eng., A* **458,** 253 (2007).
20. E. Aghion and A. Amir: Mechanical properties and environmental behavior of a magnesium alloy with a nano-/sub-micron structure. *Adv. Eng. Mater.* **9,** 747 (2007).
21. R. Baldev and M.U. Kamachi: Materials development and corrosion problems in nuclear fuel reprocessing plants. *Prog. Nucl. Energy* **48,** 283 (2006).
22. L. Zhang, Y. Han, and J. Lu: Nanocrystallization of zirconium subjected to surface mechanical attrition treatment. *Nanotechnology* **19,** 571 (2008).
23. X.Y. Zhang, M.H. Shi, C. Li, N.F. Liu, and Y.M. Wei: The influence of grain size on the corrosion resistance of nanocrystalline zirconium metal. *Mater. Sci. Eng., A* **448,** 259 (2007).
24. K.Y. Zhu, A. Vassel, F. Brisset, K. Lu, and J. Lu: Nanostructure formation mechanism of α-titanium using SMAT. *Acta Mater.* **52,** 4101 (2004).
25. X. Wu, N. Tao, Y. Hong, B. Xu, J. Lu, and K. Lu: Microstructure and evolution of mechanically-induced ultrafine grain in surface layer of Al-alloy subjected to USSP. *Acta Mater.* **50,** 2075 (2002).
26. T.G. Nieh: Hall-petch relation in nanocrystalline solids. *Scr. Mater.* **25,** 955 (1991).
27. P. Bouffioux, and L. Legras: Effect of hydriding on the residual cold work recovery and creep of Zircaloy-4 cladding tubes, in *Proceedings of the International Tropical Meeting on Light Water Reactor Fuel Performance* (Park City, UT, April 10–13, 2000).
28. D.A. Jones: *Principals and Prevention of Corrosion* (Prentice-Hall, Inc., Upper Saddle River, NJ, 1992).
29. F.J. Humphreys and M. Hatherly: *Recrystallization and Related Annealing Phenomena* (Pergamon, Oxford, 1996).
30. T.A. Hayes, M.E. Kassner, D. Amick, and R. Rosen: The thermal stability of surface deformed zirconium. *J. Nucl. Mater.* **246,** 60 (1997).
31. M. Jin, A.M. Minor, E.A. Stach, and J.W. Morris: Direct observation of deformation-induced grain growth during the nanoindentation of ultrafine-grained Al at room temperature. *Acta Mater.* **52,** 5381 (2004).
32. A.J. Haslam, D. Moldovan, V. Yamakov, D. Wolf, S.R. Phillpot, and H. Gleiter: Stress-enhanced grain growth in a nanocrystalline material by molecular-dynamics simulation. *Acta Mater.* **51,** 2097 (2003).
33. H.V. Atkinson: Overview no. 65: Theories of normal grain growth in pure single phase systems. *Acta Metall.* **36,** 469 (1988).
34. R.A. Vandermeer and H. Hsun: On the grain growth exponent of pure iron. *Acta Metall.* **42,** 3071 (1994).
35. M.P. Anderson, D.J. Srolovitz, G.S. Grest, and P.S. Sahni: Computer simulation of grain growth—I. Kinetics. *Acta Metall.* **32,** 783 (1984).
36. F. Povolo and J.C. Capitani: Influence of temperature and stress-relieving treatment of the stress relaxation in bending of zircaloy-4 near 673 K. *J. Mater. Sci.* **19,** 2969 (1984).
37. T.A. Hayes, M.E. Kassner, and R.S. Rosen: Steady-state creep of α-zirconium at temperatures up to 850°C. *Metall. Mater. Trans. A* **33,** 337 (2002).
38. K. Vieregge and C. Herzig: Grain-boundary diffusion in α-zirconium: Part I: Self-diffusion. *J. Nucl. Mater.* **173,** 118 (1990).
39. J.S. Lian, R.Z. Valifv, and B. Baudelet: On the enhanced grain growth in ultrafine grained metals. *Acta Metall. Mater.* **43,** 4165 (1995).

40. R.Z. Valiev, E.V. Kozlov, Y.F. Ivanov, J.S. Lian, A.A. Nazarov, and B. Baudlelet: Deformation behavior of ultra-fine-grained copper. *Acta Metall. Mater.* **42,** 2467 (1994).
41. J. Wang, Y. Iwahashi, Z. Horita, M. Furukawa, M. Nemoto, R.Z. Valiev, and T.G. Langdon: An investigation of microstructural stability in an Al–Mg alloy with submicrometer grain size. *Acta Mater.* **44,** 2973 (1996).
42. O. Yevtushenko, H. Natter, and R. Hempelmann: Grain-growth kinetics of nanostructured gold. *Thin Solid Films* **515,** 353 (2006).
43. H. Miyamoto, K. Yoshimura, T. Mimaki, and A. Yamashita: Behavior of intergranular corrosion of T011Y tilt grain boundaries of pure copper bicrystals. *Corros. Sci.* **44,** 1835 (2002).
44. G. Palumbo and U. Erb: Enhancing the operating life and performance of lead-acid batteries via grain-boundary engineering. *MRS Bull.* **24,** 27 (1999).
45. M.P. Hu: *Electrochemical Corrosion* (Metallurgical Industry Publishing Company, Beijing, 1991).
46. M. Pourbaix: *Atlas of Electrochemical Equilibria in Aqueous Solutions* (National Association of Corrosion Engineers, Houston, TX, 1974), p. 223.
47. L. Beaunier: Corrosion of grain boundaries: Initiation process and testing. *J. Phys. C* **43,** 6 (1982).
48. L. Beaunier, M. Froment, and C. Vignaud: A kinetical model for the electrochemical grooving of grain boundaries. *Electrochim. Acta* **25,** 1239 (1980).
49. U. Erb, H. Gleiter, and G. Schwitzgebel: The effect of boundary structure (energy) on interfacial corrosion. *Acta Metall.* **30,** 1377 (1982).
50. D.Q. Peng, X.D. Bai, X.W. Chen, Q.G. Zhou, X.Y. Liu, and P.Y. Deng: Comparison of aqueous corrosion behavior of zirconium and zircaloy-4 implanted with molybdenum. *Nucl. Instrum. Methods Phys. Res., Sect. B* **211,** 55 (2003).
51. B.A. Movchan and A.V. Demchishin: Investigations of the structure and properties of thick Ni, Ti, W, Al_2O_3 and ZrO_2 vacuum condensates. *Fiz. Met. Metalloved.* **4,** 28 (1969).
52. H.A. Johansen, G.B. Adams, and P.V. Rysselberghe: Anodic oxidation of aluminum, chromium, hafnium, niobium, tantalum, titanium, vanadium, and zirconium at very low current densities. *J. Electrochem. Soc.* **104,** 339 (1957).
53. S. Tao and D.Y. Li: Investigation of corrosion–wear synergistic attack on nanocrystalline Cu deposits. *Wear* **263,** 363 (2007).
54. S. Tao and D.Y. Li: Tribological, mechanical and electrochemical properties of nanocrystalline copper deposits produced by pulse electrodeposition. *Nanotechnology* **17,** 65 (2006).